

Spin-wave dispersion and exchange stiffness in $\text{Nd}_2\text{Fe}_{14}\text{B}$ and $R\text{Fe}_{11}\text{Ti}$ ($R=\text{Y}, \text{Nd}, \text{Sm}$) from first-principles calculations

Taro Fukazawa,^{1,2,*} Hisazumi Akai,^{3,2} Yosuke Harashima,^{1,2,4} and Takashi Miyake^{1,2}

¹*CD-FMat, National Institute of Advanced Industrial Science and Technology, Tsukuba, Ibaraki 305-8568, Japan*

²*ESICMM, National Institute for Materials Science, Tsukuba, Ibaraki 305-0047, Japan*

³*The Institute for Solid State Physics, The University of Tokyo, Kashiwa, Chiba 277-8581, Japan*

⁴*Institute of Materials and Systems for Sustainability, Nagoya University, Nagoya, Aichi 464-8601, Japan*

(Dated: December 22, 2020)

We theoretically investigate spin-wave dispersion in rare-earth magnet compounds by using first-principles calculations and a method we call the reciprocal-space algorithm (RSA). The value of the calculated exchange stiffness for $\text{Nd}_2\text{Fe}_{14}\text{B}$ is within the range of reported experimental values. We find that the exchange stiffness is considerably anisotropic when only short-range exchange couplings are considered, whereas inclusion of long-range couplings weakens the anisotropy. In contrast, $R\text{Fe}_{11}\text{Ti}$ ($R=\text{Y}, \text{Nd}, \text{Sm}$) shows large anisotropy in the exchange stiffness.

I. INTRODUCTION

Finite-temperature properties of magnetic materials are one of the central interests in the development of permanent magnets not only from a fundamental point of view but also from a technological point of view, because magnets are used at and above room temperature in industrial applications. Modern high-performance permanent magnets are rare-earth magnets, and their main phases are rare-earth transition-metal compounds. The magnet compound $\text{Nd}_2\text{Fe}_{14}\text{B}$ is the main phase of the neodymium magnet, which is often said to be the strongest magnet. $R\text{Fe}_{12}$ -type compounds with a ThMn_{12} -type structure[1] have also attracted attention as potential main phases of magnets for surpassing the neodymium magnet.

Spin-wave frequency is a fundamental quantity for studying magnetic properties at finite temperatures. It is a collective and elementary excitation in magnetic materials. The curvature of its lowest branch at the Γ point is called the spin-wave stiffness and is proportional to the exchange stiffness. Experimentally, the spin-wave stiffness can be measured directly by neutron scattering or by deduction from the magnetization curve versus temperature on basis of Bloch's $T^{3/2}$ law.

For example, the exchange stiffness of $\text{Nd}_2\text{Fe}_{14}\text{B}$ as determined by neutron scattering experiments was reported by Mayer et al.[2, 3] and by Ono et al.[4] In addition, inelastic neutron scattering was recently reported in a study by Naser et al.[5] Although Mayer et al. observed no significant difference in the spin-wave dispersion along the a direction and the c direction, Naser et al. argued that the exchange stiffness has significant anisotropy below room temperature, where the stiffness in the c direction (A_z) is smaller than in the a direction (A_x).

From a theoretical point of view, the exchange stiffness is a basic input parameter in micromagnetic simulations.

Although experimental values are used in most simulations, recent efforts have been made to determine the exchange stiffness theoretically based on first-principles calculations. Toga et al. derived a classical Heisenberg model of $\text{Nd}_2\text{Fe}_{14}\text{B}$ from the results of density functional calculations.[6] The model thus obtained was analyzed by Monte Carlo simulation to determine the exchange stiffness at finite temperatures. The exchange stiffness was found to have significant anisotropy with $A_z < A_x$. Gong et al. also performed a similar simulation and obtained a qualitatively similar result.[7, 8] However, Toga et al. noted that the anisotropy was greatly weakened when they considered more interactions between spins, which is examined in the present paper.

Previous reports on the exchange stiffness in $\text{Nd}_2\text{Fe}_{14}\text{B}$ have significant variation, ranging from 6.6 pJ/m [4] to 18 pJ/m [5]. A direct approach to spin-wave dispersion from theory can offer key information for resolving the problem by estimating the exchange stiffness from the spin-wave stiffness. There are several schemes based on first-principles calculations for spin-waves, such as those with frozen magnon approaches [9–12], those with perturbational approaches based on multiple scattering theory[13–17], and those based on direct calculations of magnetic susceptibility[18]. However, these methods are computationally heavy and do not seem to be practical for systems containing more than a few atoms in the unit cell. Pajda et al.[16] pointed out that even for bcc Fe, fcc Co, and fcc Ni, calculation of the spin-wave stiffness is time-consuming and convergence with respect to the spatial cutoff for bond lengths is very slow.

To resolve these problems, we recently developed the reciprocal-space algorithm (RSA), an accelerated computational scheme for spin-wave dispersion [19] based on Liechtenstein's method.[14] The scheme completes calculation of the dispersion without performing inverse Fourier transform to obtain the spatial representation of magnetic interactions. This optimization makes the scheme much faster, and allows it to deal with larger systems than previous methods can handle.

* E-mail: taro.fukazawa@aist.go.jp

In the present work, we apply the scheme to $\text{Nd}_2\text{Fe}_{14}\text{B}$ and $R\text{Fe}_{11}\text{Ti}$ ($R = \text{Y}, \text{Nd}, \text{Sm}$). As mentioned above, the anisotropy in the exchange stiffness has been a topic of focus in many publications.[5, 6, 8] Our results suggest that the anisotropy in $\text{Nd}_2\text{Fe}_{14}\text{B}$ is much smaller than previous results, and that it is rather isotropic. In contrast, $R\text{Fe}_{11}\text{Ti}$ exhibits significant anisotropy in its exchange stiffness in our results. We discuss this difference in anisotropy between $\text{Nd}_2\text{Fe}_{14}\text{B}$ and a ThMn_{12} -type compound in relation to differences in the unit cell. We also show the angular integrated spin-wave dispersion ($E-|q|$ dispersion) for comparison with diffraction experiments with polycrystalline and powder samples.

II. METHODOLOGY

We perform first-principles calculations based on density functional theory within the local density approximation [20, 21]. We use the Korringa-Kohn-Rostoker (KKR) Green function method. The spin-orbit coupling (SOC) is not included explicitly, but SOC for f-electrons at the rare-earth sites is implicitly considered as a trivalent open core obeying Hund's rules. The self-interaction correction[22] is also applied to those f-electrons.

We calculate magnetic couplings according to Liechtenstein's formula,[14] in which the coupling $J_{(i,a)(j,b)}$ between the i th site in the a th cell and the j th site in the b th cell is written as

$$J_{(i,a)(j,b)} = \frac{1}{4\pi} \Im \int_{-\infty}^{\epsilon_F} d\epsilon \text{Tr} \Delta_i T_{\uparrow}^{(i,a)(j,b)} \Delta_j T_{\downarrow}^{(j,b)(i,a)}, \quad (1)$$

where ϵ_F denotes the Fermi energy, $T_{\sigma}^{(i,a)(j,b)}$ is the scattering-path operator of the σ -spin electron from the (i,a) site to the (j,b) site, and Δ_i describes the spin-rotational perturbation and is defined as $\Delta_i = t_{i,\uparrow}^{-1} - t_{i,\downarrow}^{-1}$ where $t_{i,\sigma}$ denotes the t-matrix of the σ -spin potential of the i th site. Although the variables Δ_i and $T_{\sigma}^{(i,a)(j,b)}$ are functions of the angular momenta and energy, for simplicity we omitted explicitly showing these dependencies. The trace is taken with respect to the angular momenta, and the integral is with respect to the energy.

As we describe below, the Fourier transform of $J_{(i,a)(j,b)}$ is needed for calculating the spin-wave dispersion:

$$J_{i,j}(\vec{q}) = \frac{1}{N} \sum_a J_{(i,0)(j,a)} e^{-i\vec{q}\cdot(\vec{R}_a - \vec{R}_0)}, \quad (2)$$

where \vec{R}_a denotes the position of the a th cell. We directly calculate $J_{i,j}(\vec{q})$ in reciprocal space. This benefits the precision because the KKR scheme involves calculation of the scattering-path operator in reciprocal space, and transformation of the operator into real space introduces additional errors. However, the perturbation Δ_i is a δ -like local quantity, and can be transformed to reciprocal space without any loss of precision: $\Delta_i(\vec{q}) = \Delta_i$. The

transformed expression of Eq. (1) is as follows:

$$J_{i,j}(\vec{q}) = \frac{1}{4\pi} \Im \sum_{\vec{k}} \int_{-\infty}^{\epsilon_F} d\epsilon \text{Tr} \Delta_i T_{\uparrow}^{i,j}(\vec{k} + \vec{q}) \Delta_j T_{\downarrow}^{j,i}(\vec{k}). \quad (3)$$

We can construct the classical Heisenberg model by using the values of $J_{(i,a)(j,b)}$ as follows:

$$H = - \sum_{l=(a,i)} \sum_{\substack{m=(b,j) \\ m \neq l}} J_{lm} \vec{e}_l \cdot \vec{e}_m, \quad (4)$$

where \vec{e} denotes the unit vector that indicates the direction of the spin moment of the site. We fix the spin moment S_i to the value at the ground state, and thus the spin vector is $\vec{S}_{(a,i)} = S_i \vec{e}_{(a,i)}$. We renormalize the magnetic coupling into the form $\tilde{J}_{(a,i)(b,j)} = J_{(a,i)(b,j)} / (S_i S_j)$. As a result, the Hamiltonian is cast into the form

$$H = - \sum_{l=(a,i)} \sum_{m=(b,j)} \tilde{J}_{lm} \vec{S}_l \cdot \vec{S}_m. \quad (5)$$

Based on the semi-classical treatment[9], the energy of spin-waves for a wave vector \vec{q} can be obtained as eigenvalues of the matrix in which the (i,j) component is

$$F_{ij}(\vec{q}) = 2\delta_{i,j} \sum_k S_k \tilde{J}_{i,k}(\vec{0}) - 2S_i \tilde{J}_{i,j}(\vec{q}) \quad (6)$$

$$= 2\delta_{i,j} \sum_k J_{i,k}(\vec{0}) / S_i - 2J_{i,j}(\vec{q}) / S_j. \quad (7)$$

We obtain the spin-wave dispersion by diagonalizing this matrix using the values of J calculated by Eq. (3).

We calculate the spin-wave stiffness by fitting a quadratic function from the curvature of the lowest branch around the Γ point. To compare the RSA with the spatial method, the spin-wave stiffness is also estimated by the following matrix, which is valid when $q \ll 1$:

$$F_{ij}(\vec{q}) \simeq \frac{2}{S_j N} \sum_a \left(\delta_{ij} \sum_k J_{(i,0)(k,a)} - J_{(i,0)(j,a)} \right) - \sum_a J_{(i,0)(j,a)} \left(i\vec{q} \cdot (\vec{R}_a - \vec{R}_0) + \frac{1}{2} |\vec{q} \cdot (\vec{R}_a - \vec{R}_0)|^2 \right). \quad (8)$$

However, this estimate is numerically unstable because the Fourier interpolation confines the curve onto the given points and errors in $F_{ij}(\vec{q})$ generate fictitious high harmonics, which directly lead to errors in the curvature. In contrast, the quadratic regression that we use is more robust against the errors. In addition, we do not have to calculate the spatial $J_{(i,a)(j,b)}$ and do not need to consume memory to store them. Although calculation of the convolution in Eq. (3) is straightforward, it is also possible to use the fast Fourier transform to calculate $F_{ij}(\vec{q})$ when there is enough memory.

These methods are applied to $\text{Nd}_2\text{Fe}_{14}\text{B}$ [space group: $P4_2/mmm$ (#136)] and $R\text{Fe}_{11}\text{Ti}$ ($R = \text{Y}, \text{Nd}, \text{Sm}$). The

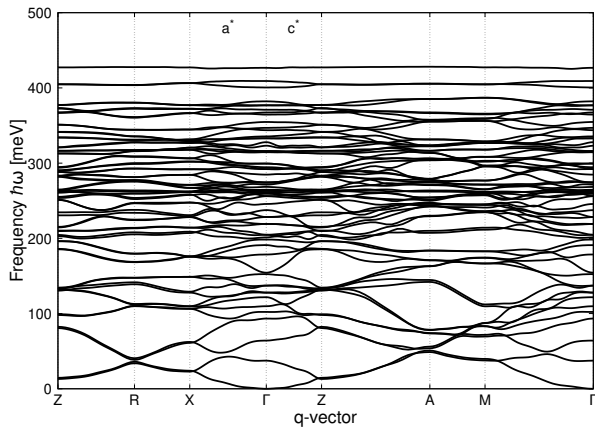


FIG. 1. Spin-wave dispersion for $\text{Nd}_2\text{Fe}_{14}\text{B}$.

latter systems are obtained by replacing one of the Fe(8i) sites with Ti in $R\text{Fe}_{12}$ having the ThMn_{12} structure [space group: $I4/mmm$ (#139)]. We adopt lattice parameters from previous studies obtained by numerical optimization using first-principles calculations. The parameters for $\text{Nd}_2\text{Fe}_{14}\text{B}$ are taken from Ref. 23, and those for $R\text{Fe}_{11}\text{Ti}$ are from Ref. 24.

III. RESULTS AND DISCUSSION

The above-mentioned scheme enables us to calculate the spin-wave dispersion of $\text{Nd}_2\text{Fe}_{14}\text{B}$, which contains 68 atoms in a unit cell. Figure 1 shows the calculated results. Although this scheme can give branches associated with high excitation energy, we should focus on low-energy excitations when comparing these results with experimental ones because the Heisenberg model we used in the calculation is not valid for describing excitations with high energy transfer. We hereafter discuss the lowest branch of spin waves around the Γ point through its spin-wave stiffness.

Table I shows the spin-wave stiffness D for $\text{Nd}_2\text{Fe}_{14}\text{B}$. The curvature of the lowest branch around the Γ point along the a^* axis (D_a), along the b^* axis (D_b) and along the c^* axis (D_c) are also shown in the table. The spin-wave stiffness is converted to exchange stiffness by the following equation:[19]

$$A_{i'} = \rho D_i / 4 \quad [(i, i') = (a, x), (b, y), (c, z)], \quad (9)$$

where ρ is the number of Bohr magnetons per unit-cell volume.

The exchange stiffness A and the components in the x -, y - and z -direction (A_x , A_y and A_z , respectively) are shown in Table II. These results are within the range of experimental values by Ono et al. (6.6 pJ/m) and Naser et al. (18 pJ/m) for $\text{Nd}_2\text{Fe}_{14}\text{B}$.

In our results, the anisotropy ratio A_z/A_x of the exchange stiffness is approximately 1.1. Our prediction is much more isotropic than Monte Carlo simulations with

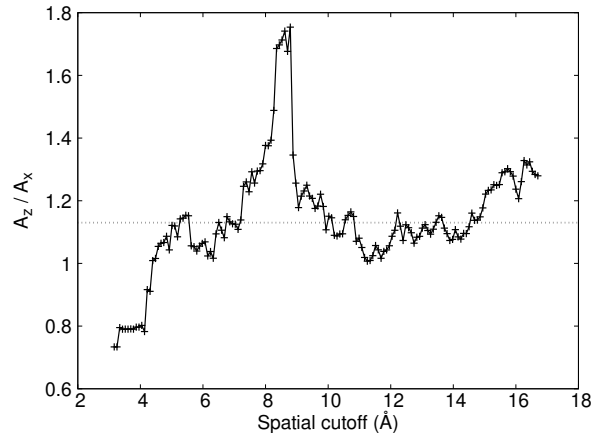


FIG. 2. Anisotropy in the exchange stiffness for $\text{Nd}_2\text{Fe}_{14}\text{B}$ calculated by Eq. (8). The horizontal axis shows the spatial cutoff for J_{ij} . The horizontal dotted line shows the anisotropy ratio obtained by the RSA calculation.

TABLE I. Values of spin-wave stiffness D for $\text{Nd}_2\text{Fe}_{14}\text{B}$, $R\text{Fe}_{11}\text{Ti}$, and SmFe_{12} . D_a is the curvature along the a^* axis of the bottom branch around the Γ point, D_b along the b^* axis, and D_c along the c^* axis. The values are in units of $\text{meV}\text{\AA}^2$.

Formula	D_a	D_b	D_c	$D = \sqrt[3]{D_a D_b D_c}$
$\text{Nd}_2\text{Fe}_{14}\text{B}$	190	190	215	198
YFe_{11}Ti	117	167	249	170
$\text{NdFe}_{11}\text{Ti}$	178	158	262	195
$\text{SmFe}_{11}\text{Ti}$	172	168	271	199
SmFe_{12} [19]	91.6	91.6	194	118 ($\text{meV}\text{\AA}^2$)

ab initio modeling, which gave $A_z/A_x \sim 0.8$ at the lowest temperature.[6, 8] This deviation can be attributed to their use of spatial J_{ij} . Figure 2 shows the anisotropy ratio calculated by diagonalizing the approximate F_{ij} of Eq. (8) while varying the cutoff on the i - j distance. At the spatial cutoff of 3.5 \AA , which is the value used in Ref. 6, the value of A_x becomes larger than A_z and the anisotropy is inversely overestimated due to the artificial cutoff. Note that RSA does not have this kind of spatial cutoff. Our results using RSA support the experimental observation by Mayer et al.[3] that there are no identifiable differences between the dispersion along the a^* and c^* axis although they did not quantitatively estimate the isotropy.

We also show the values of stiffness for $R\text{Fe}_{11}\text{Ti}$ in Tables I and II. The Ti element is located at the Fe(8i) site of $R\text{Fe}_{12}$ that is next to the R atom along the a axis, as in the notation of Harashima et al.[24] The unit cell is orthorhombic, and the curvatures along the a and b axes do not coincide by symmetry. In these $R\text{Fe}_{12}$ systems, the stiffness along the c axis is significantly larger than along the a and b axes, which has also been seen in $\text{Sm}(\text{Fe},\text{Co})_{12}$.[19]

We previously reported in Ref. 19 that distortion of the

TABLE II. Values of exchange stiffness A for $\text{Nd}_2\text{Fe}_{14}\text{B}$, $R\text{Fe}_{11}\text{Ti}$ and SmFe_{12} . A_x is the exchange stiffness associated with spin waves along the x axis, A_y along the y axis, and A_z along z axis. The values are in units of pJ/m .

Formula	A_x	A_y	A_z	$A = \sqrt[3]{A_x A_y A_z}$
$\text{Nd}_2\text{Fe}_{14}\text{B}$	10.3	10.3	11.7	10.7
YFe_{11}Ti	5.7	8.1	12.1	8.3
$\text{NdFe}_{11}\text{Ti}$	10.0	8.9	14.7	10.9
$\text{SmFe}_{11}\text{Ti}$	8.6	8.4	13.5	9.9
SmFe_{12} [19]	5.6	5.6	7.2	11.9 (pJ/m)

Bravais lattice has an effect on the anisotropy of the spin-wave stiffness even when the values of J_{ij} are fixed. In the case of the transformations $a \rightarrow \alpha a$ and $c \rightarrow \gamma c$, the $D_c/D_a (\equiv R)$ value is transformed to $(\gamma/\alpha)^2 R$ by the distortion. This must not be confused with taking a supercell, which involves band folding but does not change the curvatures. It is noteworthy that the conventional cell of $\text{Nd}_2\text{Fe}_{14}\text{B}$ stacked 3 times along the c axis ($a = 8.791 \text{ \AA}$, $c = 36.42 \text{ \AA}$, $D_c/D_a = 1.1$) has a similar length to the conventional cell of SmFe_{12} stacked 8 times along the c axis ($a = 8.533 \text{ \AA}$, $c = 37.45 \text{ \AA}$, $D_c/D_a = 1.3$). The lengths of SmFe_{12} become identical to $\text{Nd}_2\text{Fe}_{14}\text{B}$ when a tetragonal distortion of $\alpha = 1.03$ and $\gamma = 0.97$ is applied to SmFe_{12} . This distortion multiplies the factor of $(\gamma/\alpha)^2 = 0.89$ to the anisotropy ratio, D_c/D_a , and makes the ratio more isotropic: $R = 1.2$, which corresponds to $\text{Nd}_2\text{Fe}_{14}\text{B}$.

To visualize the anisotropy, we calculate angular integrated spin-wave dispersions according to Eq. (B13) in Appendix B. Figure 3 shows the density of states for $\text{Nd}_2\text{Fe}_{14}\text{B}$ and $R\text{Fe}_{11}\text{Ti}$ as functions of the absolute value, q , of the wave vector and the energy, E . These dispersions correspond to diffraction of polycrystalline and powder samples. As mentioned in Appendix B, the lower edge of the finite-DOS region is given by $E = D_{\min} q^2$ and the upper edge by $E = D_{\max} q^2$, where $D_{\min} = \min(D_a, D_b, D_c)$ and $D_{\max} = \max(D_a, D_b, D_c)$. Therefore, the anisotropy of the spin-wave stiffness is reflected in the smearing of the dispersion in these figures. The smearing in $\text{Nd}_2\text{Fe}_{14}\text{B}$ is much smaller than the measurement errors in the neutron scattering experiment by Ono et al.[4]. Hawaii et al. recently performed inelastic neutron diffraction experiments for $R\text{Fe}_{11}\text{Ti}$. [25] Although anisotropy could not be seen in their data due to uncertainties in the experiment, further development of neutron scattering techniques will hopefully resolve the existence of the anisotropy.

IV. CONCLUSION

We presented the spin-wave dispersion for $\text{Nd}_2\text{Fe}_{14}\text{B}$ and $R\text{Fe}_{11}\text{Ti}$ obtained using first-principles calculations. Our recently developed RSA, an accelerated scheme for

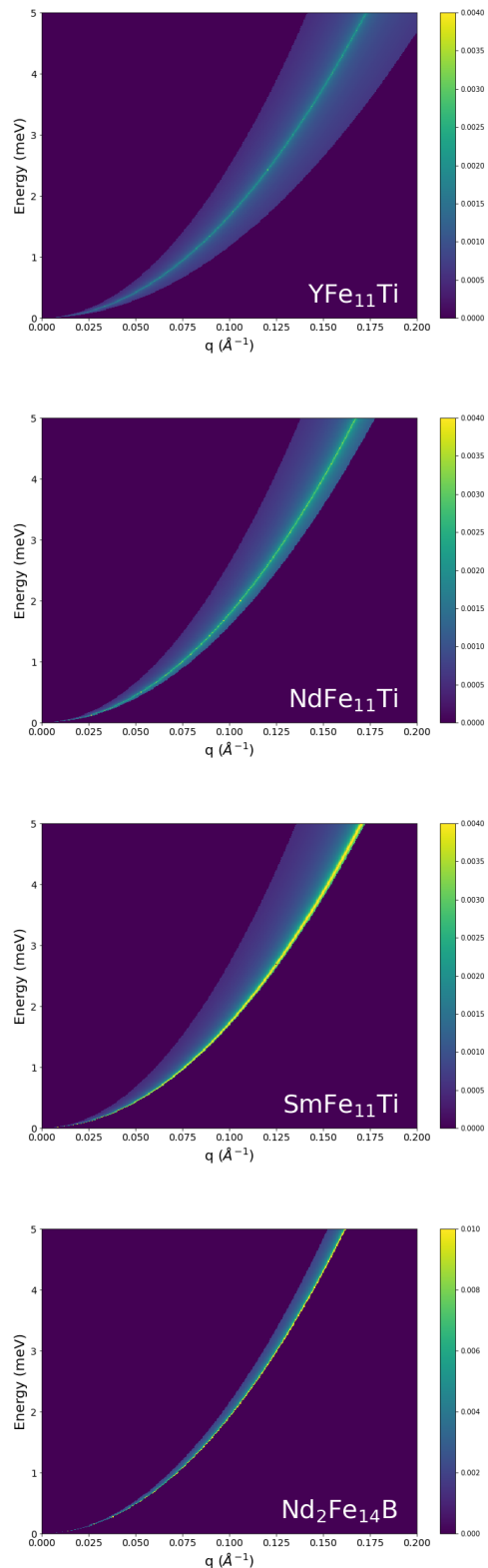


FIG. 3. (Color online) Angular-integrated spin-wave dispersion for $R\text{Fe}_{11}\text{Ti}$ and $\text{Nd}_2\text{Fe}_{14}\text{B}$. These color maps show the density of states $I(q, E)$ of Eq. (B13) where the horizontal axis denotes the absolute value of a wave vector, q , and the vertical axis is the energy, E .

spin-wave dispersion that is based on the Liechtenstein formula and its use in reciprocal space, enabled these calculations in practical time. We discuss the anisotropy of the exchange stiffness in $\text{Nd}_2\text{Fe}_{14}\text{B}$. Our results suggest that the anisotropy in the exchange stiffness of $\text{Nd}_2\text{Fe}_{14}\text{B}$ is much smaller than the values obtained by previous Monte Carlo simulations. We also demonstrated that the spatial cutoff can be a crucial factor in the precision when estimating the anisotropy. However, RFe_{11}Ti has a strong anisotropy in our estimation of the spin-wave stiffness. We also showed the angular integrated dispersion of the spin-waves, which corresponds to diffraction of polycrystalline and powder samples. We pointed out that the anisotropy can be seen as smearing of the E - q dispersion, and this is comparable with neutron scattering experiments.

ACKNOWLEDGMENT

We are grateful to Takafumi Hawai, Kanta Ono, and Nobuya Sato for their advice and fruitful discussions. We acknowledge support from the Elements Strategy Initiative Center for Magnetic Materials (ESICMM), Grant Number JPMXP0112101004, under the auspices of the Ministry of Education, Culture, Sports, Science and Technology (MEXT). This work was also supported by MEXT through the ‘‘Program for Promoting Researches on the Supercomputer Fugaku’’ (DPMSD). The computation was partly conducted using the facilities of the Supercomputer Center at the Institute for Solid State Physics, University of Tokyo, and the supercomputer of the Academic Center for Computing and Media Studies (ACCMS), Kyoto University. This research also used computational resources of the K computer provided by the RIKEN Advanced Institute for Computational Science through the HPCI System Research project (Project ID:hp170100).

Appendix A: Convergence with respect to the number of k points in Fe and Co

We examine the convergence of the calculation for bcc-Fe and hcp-Co with respect to the number of k -points. Figure 4 shows the spin-wave dispersion obtained by our calculation. The solid lines are for the calculations with the largest number of k -points. The overall behavior of the curve agrees with previous studies[9, 16]. The dashed curves show the results with a smaller number of k -points, and the dash-dotted curves with an even smaller number.

In the case of Fe, we need a large number of k -points to reproduce the description of the spin-wave dispersion with $18 \times 18 \times 18$ k -points (solid). The dot-dashed curve shows the dispersion with $8 \times 8 \times 8$ k -points (dot-dashed), which is the cheapest calculation among the three and has a significant deviation from the solid curve. With

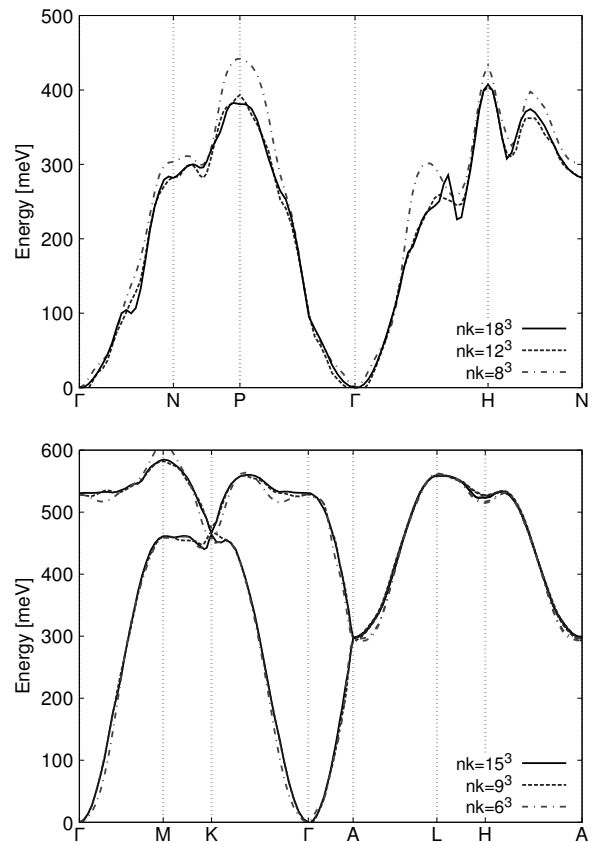


FIG. 4. Spin-wave dispersion in (Top) bcc-Fe and (Bottom) hcp Co. The solid lines are from the calculations with the largest number of k -points (nk): $18 \times 18 \times 18$ for Fe; $15 \times 15 \times 15$ for Co. The dashed lines and the dash-dot lines are for smaller nk .

$12 \times 12 \times 12$ k -points (dashed), some features such as the depth of the dip on the Γ -H line are missing. However, we confirmed that the curves with $14 \times 14 \times 14$ k -points appear much closer to the solid curve. In the case of Co, convergence is much faster owing to the smallness of the Brillouin zone, and $9 \times 9 \times 9$ k -points seem to be enough.

Figure 5 shows the convergence of the spin-wave stiffness—the curvature around the Γ point in the lowest branch—with respect to the number of k -points. The filled circles show the results when the SCF potential was obtained with the same number of k -points as used in the spin-wave calculation. The spin-wave stiffness appears well-behaved as a function of the number of k -points and converges rapidly. We also show the results for the SCF potential fixed to that obtained with $10 \times 10 \times 10$ k -points as open circles. By comparison, we observe that the quality of the potential does not have much effect on the spin-wave stiffness.

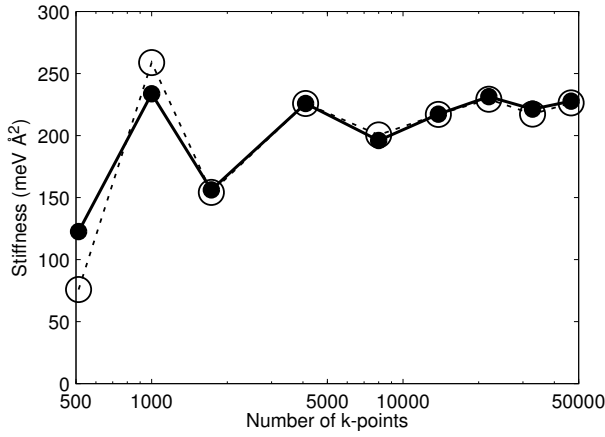


FIG. 5. Convergence of the spin-wave stiffness with respect to the number of the k -points (nk) where nk for SCF is the same as the spin-wave calculation (filled circle), and where nk is fixed to 1000 (open circle). Note that the horizontal axis is in log scale.

Appendix B: E - q dispersion of spin-waves

To compare the theoretical results with experimental results for polycrystalline and powder samples, we perform angular integration of the following energy dispersion:

$$E = D_a q_a^2 + D_b q_b^2 + D_c q_c^2 \quad (0 \leq D_a \leq D_b \leq D_c), \quad (\text{B1})$$

which is adequate when the low-energy excitations are of interest. The inequality for the coefficients does not deteriorate the generality because it is always satisfied by exchanging the labels of axes.

It is obvious that there are states only when $D_a q^2 \leq E \leq D_c q^2$ holds. We divide the problem into 3 cases: (i) $D_a q^2 \leq E < D_b q^2$, (ii) $E = D_b q^2$, and (iii) $D_b q^2 < E \leq D_c q^2$. In the case of (i), by eliminating q_a^2 in E with $q_a^2 = q^2 - q_b^2 - q_c^2$, we can obtain

$$\frac{x^2}{\alpha^2} + \frac{y^2}{\beta^2} = \epsilon^2 \quad (0 < \alpha \leq \beta), \quad (\text{B2})$$

$$z^2 = q^2 - x^2 - y^2, \quad (\text{B3})$$

with

$$\alpha = \sqrt{\frac{1}{D_c - D_a}}, \quad \beta = \sqrt{\frac{1}{D_b - D_a}}, \quad \epsilon = \sqrt{E - D_a q^2}, \quad (\text{B4})$$

$$x = q_c, \quad y = q_b, \quad z = q_a. \quad (\text{B5})$$

In the case of (ii), we can immediately obtain

$$(D_b - D_a)q_a^2 = (D_c - D_b)q_c^2 \quad (\text{B6})$$

by eliminating q_b in E . In the case of (iii), by eliminating q_c^2 in E with $q_c^2 = q^2 - q_a^2 - q_b^2$, we can obtain the same

set of equations as Eq. (B2) and Eq. (B3) with

$$\alpha = \sqrt{\frac{1}{D_c - D_a}}, \quad \beta = \sqrt{\frac{1}{D_c - D_b}}, \quad \epsilon = \sqrt{D_c q^2 - E}, \quad (\text{B7})$$

$$x = q_a, \quad y = q_b, \quad z = q_c. \quad (\text{B8})$$

Therefore, we can express the equations for the possible sets of q_a, q_b, q_c by a single set of equations—Eq. (B2) and Eq. (B3)—except for the singular point at which (ii) $E = D_b q^2$ holds.

When considering the density of states of spin-waves, we can disregard case (ii) because it has a measure of zero in the integral with respect to energy. Let us consider a solution $\vec{P} = (x, y, z)$ of (B2) and (B3) in the $z > 0$ region. By the following transform:

$$x = \epsilon \alpha \cos \theta, \quad (\text{B9})$$

$$y = \epsilon \beta \sin \theta, \quad (\text{B10})$$

this vector can be expressed as follows:

$$\vec{P} = \left(\epsilon \alpha \cos \theta, \epsilon \beta \sin \theta, \sqrt{q^2 - \epsilon^2 (\alpha^2 \cos^2 \theta + \beta^2 \sin^2 \theta)} \right). \quad (\text{B11})$$

When ΔE and Δq are infinitesimal numbers, the number of states within the energy range from E to $E + \Delta E$ and within the momentum range from q to $q + \Delta q$ can be expressed as

$$I(q, E) \Delta E \Delta q = \frac{2V}{8\pi^3} \int_{-\pi}^{\pi} d\theta \left| \frac{\partial(x, y, z)}{\partial(q, E, \theta)} \right| \Delta E \Delta q \quad (\text{B12})$$

where V denotes the system volume. The factor of two is necessary because there is another solution $(x, y, -z)$ in $z < 0$. By straightforward calculation, we can obtain an expression with the complete elliptic integral of the first kind, $K(k)$, as follows:

$$I(q, E) = \frac{V}{\pi^3} \alpha \beta \frac{q}{\sqrt{q^2 - \epsilon^2 \alpha^2}} K \left(\sqrt{\frac{(\beta^2 - \alpha^2) \epsilon^2}{q^2 - \epsilon^2 \alpha^2}} \right), \quad (\text{B13})$$

An outline of this is shown in Fig. 6. Although we can also write the elliptic modulus, $k = \sqrt{(\beta^2 - \alpha^2) \epsilon^2 / (q^2 - \epsilon^2 \alpha^2)}$, in terms of the variables in Eq. (B1), the expressions for cases (i) and (iii) are different:

$$k^2 = (\beta^2 - \alpha^2) \epsilon^2 / (q^2 - \epsilon^2 \alpha^2) = \begin{cases} \frac{D_c - D_b}{D_c q^2 - E} \frac{E - D_a q^2}{D_b - D_a} & \text{Case (i)} \\ \frac{D_b - D_a}{E - D_a q^2} \frac{D_c q^2 - E}{D_c - D_b} & \text{Case (iii)} \end{cases}, \quad (\text{B14})$$

with which one can observe $0 \leq k^2 < 1$. When E is fixed, k is a monotonically increasing function of q in case (i) while k is monotonically decreasing in case (iii).

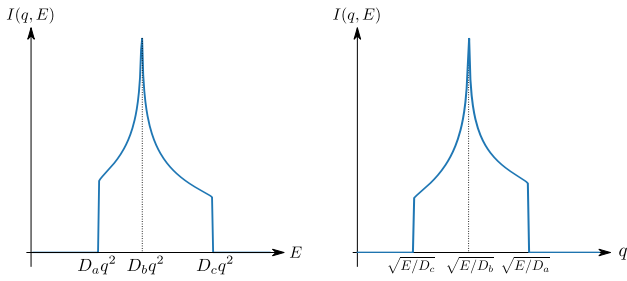


FIG. 6. Outlines of $I(q, E)$ in Eq. (B13) where (Left) q is fixed and (Right) E is fixed.

Because $K(k)$ is also a monotonically increasing function, we observe

$$I(E) \leq \lim_{E \rightarrow D_b q^2} I(E) = I(D_b q^2). \quad (\text{B15})$$

Therefore, the density of states is most intense along the line of $E = D_b q^2$.

-
- [1] Y Hirayama, Y K Takahashi, S Hirose, and K Hono, “Intrinsic hard magnetic properties of $\text{Sm}(\text{Fe}_{1-x}\text{Co}_x)_{12}$ compound with the ThMn_{12} structure,” *Scripta Materialia* **138**, 62–65 (2017).
- [2] HM Mayer, M Steiner, N Stüßler, H Weinfurter, K Kakurai, B Dorner, Per-Anker Lindgård, KN Clausen, S Hock, and W Rodewald, “Inelastic neutron scattering measurements on $\text{Nd}_2\text{Fe}_{14}\text{B}$ single crystals,” *Journal of Magnetism and Magnetic Materials* **97**, 210–218 (1991).
- [3] HM Mayer, M Steiner, N Stüßler, H Weinfurter, B Dorner, Per-Anker Lindgård, KN Clausen, S Hock, and R Verhoef, “Inelastic neutron scattering measurements on $\text{Nd}_2\text{Fe}_{14}\text{B}$ and $\text{Y}_2\text{Fe}_{14}\text{B}$ single crystals,” *Journal of Magnetism and Magnetic Materials* **104**, 1295–1297 (1992).
- [4] K Ono, N Inami, K Saito, Y Takeichi, M Yano, T Shoji, A Manabe, A Kato, Y Kaneko, D Kawana, *et al.*, “Observation of spin-wave dispersion in Nd-Fe-B magnets using neutron Brillouin scattering,” *Journal of Applied Physics* **115**, 17A714 (2014).
- [5] H Naser, C Rado, G Lapertot, and S Raymond, “Anisotropy and temperature dependence of the spin-wave stiffness in $\text{Nd}_2\text{Fe}_{14}\text{B}$: An inelastic neutron scattering investigation,” *Physical Review B* **102**, 014443 (2020).
- [6] Yuta Toga, Masamichi Nishino, Seiji Miyashita, Takashi Miyake, and Akimasa Sakuma, “Anisotropy of exchange stiffness based on atomic-scale magnetic properties in the rare-earth permanent magnet $\text{Nd}_2\text{Fe}_{14}\text{B}$,” *Physical Review B* **98**, 054418 (2018).
- [7] Qihua Gong, Min Yi, Richard F. L. Evans, Bai-Xiang Xu, and Oliver Gutfleisch, “Calculating temperature-dependent properties of $\text{Nd}_2\text{Fe}_{14}\text{B}$ permanent magnets by atomistic spin model simulations,” *Phys. Rev. B* **99**, 214409 (2019).
- [8] Qihua Gong, Min Yi, Richard F. L. Evans, Oliver Gutfleisch, and Bai-Xiang Xu, “Anisotropic exchange in Nd-Fe-B permanent magnets,” *Materials Research Letters* **8**, 89–96 (2020), <https://doi.org/10.1080/21663831.2019.1702116>.
- [9] S V Halilov, H Eschrig, A Y Perlov, and P M Oppeneer, “Adiabatic spin dynamics from spin-density-functional theory: Application to Fe, Co, and Ni,” *Physical Review B* **58**, 293 (1998).
- [10] M Van Schilfgaarde and VP Antropov, “First-principles exchange interactions in Fe, Ni, and Co,” *Journal of applied physics* **85**, 4827–4829 (1999).
- [11] S. Shallcross, A. E. Kissavos, V. Meded, and A. V. Ruban, “An ab initio effective hamiltonian for magnetism including longitudinal spin fluctuations,” *Phys. Rev. B* **72**, 104437 (2005).
- [12] P. Yu, X. F. Jin, J. Kudrnovský, D. S. Wang, and P. Bruno, “Curie temperatures of fcc and bcc nickel and permalloy: Supercell and green’s function methods,” *Phys. Rev. B* **77**, 054431 (2008).
- [13] T. Oguchi, K. Terakura, and A. R. Williams, “Band theory of the magnetic interaction in mno, mns, and nio,” *Phys. Rev. B* **28**, 6443–6452 (1983).
- [14] A I Liechtenstein, M I Katsnelson, V P Antropov, and V A Gubanov, “Local spin density functional approach to the theory of exchange interactions in ferromagnetic metals and alloys,” *Journal of Magnetism and Magnetic Materials* **67**, 65–74 (1987).
- [15] ON Mryasov, Arthur J Freeman, and AI Liechtenstein, “Theory of non-heisenberg exchange: Results for localized and itinerant magnets,” *Journal of applied physics* **79**, 4805–4807 (1996).
- [16] Marek Pajda, J Kudrnovský, I Turek, Vaclav Drchal, and Patrick Bruno, “Ab initio calculations of exchange interactions, spin-wave stiffness constants, and Curie temperatures of Fe, Co, and Ni,” *Physical Review B* **64**, 174402 (2001).
- [17] O. Šipr, S. Mankovsky, and H. Ebert, “Spin wave stiffness and exchange stiffness of doped permalloy via ab initio calculations,” *Phys. Rev. B* **100**, 024435 (2019).
- [18] H Okumura, K Sato, and T Kotani, “Spin-wave dispersion of 3 d ferromagnets based on quasiparticle self-consistent g w calculations,” *Physical Review B* **100**, 054419 (2019).
- [19] Taro Fukazawa, Hisazumi Akai, Yosuke Harashima, and Takashi Miyake, “First-principles study of spin-wave dispersion in $\text{Sm}(\text{Fe}_{1-x}\text{Co}_x)_{12}$,” *Journal of Magnetism and Magnetic Materials* **469**, 296–301 (2019).
- [20] Pierre Hohenberg and Walter Kohn, “Inhomogeneous electron gas,” *Physical Review* **136**, B864 (1964).
- [21] Walter Kohn and Lu Jeu Sham, “Self-consistent equations including exchange and correlation effects,” *Physical Review* **140**, A1133 (1965).

- [22] J. P. Perdew and Alex Zunger, “Self-interaction correction to density-functional approximations for many-electron systems,” *Phys. Rev. B* **23**, 5048–5079 (1981).
- [23] Yasutomi Tatetsu, Yosuke Harashima, Takashi Miyake, and Yoshihiro Gohda, “Role of typical elements in $\text{Nd}_2\text{Fe}_{14}X$ ($X = \text{B}, \text{C}, \text{N}, \text{O}, \text{F}$),” *Phys. Rev. Materials* **2**, 074410 (2018).
- [24] Yosuke Harashima, Kiyoyuki Terakura, Hiori Kino, Shoji Ishibashi, and Takashi Miyake, “First-principles study of structural and magnetic properties of $\text{R}(\text{Fe},\text{Ti})_{12}$ and $\text{R}(\text{Fe},\text{Ti})_{12}\text{N}$ ($\text{R} = \text{Nd}, \text{Sm}, \text{Y}$),” in *Proceedings of Computational Science Workshop 2014 (CSW2014)*, JPS Conference Proceedings, Vol. 5 (2015) p. 1021.
- [25] Takafumi Hawai, Masao Yano, Tetsuya Shoji, Hiraku Saito, Tetsuya Yokoo, Shinichi Itoh, and Kanta Ono, “Spin-wave for material design of rare-earth magnets,” private communication.